International Journal of Heat and Mass Transfer 119 (2018) 614–623

Contents lists available at ScienceDirect

International Journal of Heat and Mass Transfer

journal homepage: www.elsevier.com/locate/ijhmt

Quantitative prediction of oxide inclusion defects inside the casting and on the walls during cast-filling processes

Liu Cao, Fei Sun *, Tao Chen, Yulong Tang, Dunming Liao

State Key Laboratory of Materials Processing and Die & Mould Technology, Huazhong University of Science and Technology, Wuhan 430074, China

ARTICLE INFO

Article history:
Received 6 May 2017
Received in revised form 16 October 2017
Accepted 27 November 2017

Keywords:
Oxide inclusion
Formation rate
Wall adhesion
Quantitative prediction
Cast-fillingprocess
OpenFOAM

ABSTRACT

Oxide inclusions are a common defect in casting production, but their formation and evolution processes are difficult to directly observe experimentally. To accurately predict these, one should calculate the formation rate of the oxide inclusion as well as its wall adhesion. Here, we propose a formation rate model that is relevant to the volume fraction of liquid metal, the temperature, and the current oxide inclusion density. A boundary condition was developed to handle the adhesion and accumulation on the wall; thus, a quantitative indicator is available to directly obtain the content of the oxide inclusion defects on different parts. We used the open source computational fluid dynamics (CFD) software OpenFOAM to predict oxide inclusion defects inside the casting and on the walls during cast-filling processes. A representative aluminum alloy-casting technology was simulated to analyze the effects of different runner systems on the oxide inclusion distributions inside casting and on the wall. The simulation results largely coincide with experimental data from the literature. A practical copper alloy-casting technology was then calculated, and the simulation results of the oxide inclusion defects are consistent with the actual casting defect distribution. This confirms the utility of the model.

1. Introduction

Oxide inclusions are a common defect in casting production. They can significantly decrease the surface accuracy of the casting and can even lead to cracking and casting scraps [1–3]. At the beginning of the filling process, a paper-thin oxide film is instantly generated on the liquid front due to the good oxidation capacity of the liquid metal. This becomes thicker over time. During the filling process, some of the oxide film adheres to the wall of the mold and accumulates—this affects the surface quality of the casting. Other oxide films are drawn into the liquid metal to form oxide inclusions that are the base of heterogeneous nucleation. This impedes the cast feeding, and induces gas pore, resulting shrinkage porosity, inferior mechanical properties of the casting, and even fatigue cracking during use [5,6].

Fig. 1 presents secondary electron images of the two opposing surfaces of an aluminum alloy tensile fracture [4]. The crack was initiated in the oxide film inside the casting. Current experimental measures can only analyze the final oxide inclusion distribution of the casting. This makes it difficult to directly observe the formation and evolution of the oxide inclusion. Thus, numerical simulation plays an important role. The formation of the oxide inclusion is a complex chemical reaction and oxide inclusions easily adhere to the wall of mold. Thus, accurately predicting the defect involves calculating the formation rate of the oxide inclusion as well as its adhesion; unfortunately, correlational studies remain preliminary. Therefore, quantitative models that optimize the casting technology and improve the overall casting performance could have a large impact.

There has been a recent increase in studies that numerically predict oxide inclusion defects during cast filling. Many distinctive simulation methods have been developed [7–13]. These can be divided into the following three categories.

(1) Criterion model

Lai et al. [14] considered the "surplus" free surface area—the area difference between the transient free surface generated by the turn-up free surface and the free surface generated during the smooth filling process—to be the criterion of oxide inclusion involvement. More "surplus" free surface area resulted in oxide inclusion being more likely. This simulation method only considers oxide inclusions near the free surface. It does not track the subsequent movement of oxide inclusions with liquid metal. Thus, the final distribution of oxide inclusions cannot be predicted. In

* Corresponding author.
E-mail address: fsun@hust.edu.cn (F. Sun).

https://doi.org/10.1016/j.ijheatmasstransfer.2017.11.127
0017-9310/

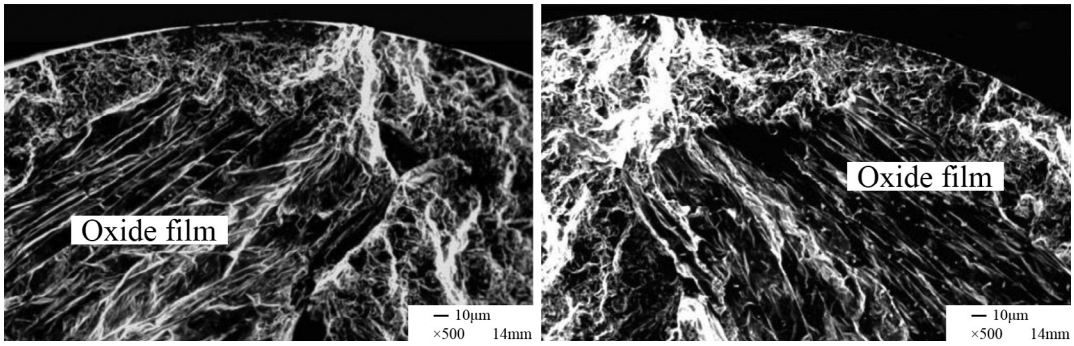

Fig. 1. Secondary electron images of the two opposing surfaces of an aluminum alloy tensile fracture [4].

addition, it is difficult to confirm the free surface area during smooth filling when the casting geometric shape is complex.

(2) Scalar model

A scalar field can record the oxide inclusion distribution in a scalar model. The movement of an oxide inclusion with liquid metal was calculated via the transport equation. This can be used to calculate the oxide inclusion distribution inside the casting. The difference between the scalar models is the formation rate model of the oxide inclusion. Barkhudarov et al. [15] showed that the formation of an oxide inclusion on a free surface gradually accumulated with a wavy deformation and the folding of an inordinate free surface. This showed an increasing trend at a constant speed. Backer et al. [16] used the experimental results [5] of Campbell to study the oxide inclusion formation, and showed that the oxide inclusion could be generated with an inordinate free surface when the free surface velocity of an aluminum alloy liquid metal exceeded 0.5 m/s. This simulation method can track the movement of an oxide inclusion with the liquid metal. Thus, the final distribution of the oxide inclusion can be predicted, but the oxide inclusion distribution on the wall cannot be calculated because it fails to account for the adhesion phenomenon between the oxide inclusion and the wall of the mold.

(3) Eulerian-Lagrangian model

The Eulerian-Lagrangian model combines the macroscopic fluid model with a discrete particle dynamic model. It replaces the oxide inclusion with discrete particles. Reilly et al. [17] adopted a particle tracking method to judge the involvement of an oxide inclusion near the free surface with a Boolean Logic Criteria. Xu et al. [18] calculated the movement process and the locations of liquid metal and inclusions injected into the mold. This used two dimensions and the Eulerian-Lagrangian model. The results were verified by water simulation experiments.

Dai et al. [19] described the movement of oxide inclusions on a free surface by the Lagrangian-VOF method. They then developed a two-dimensional Oxide Film Entrainment Tracking algorithm to calculate the liquid aluminum flow and movement as well as the folding and entrapment of oxide inclusions during mold filling. This simulation method can explicitly track the movement of oxide inclusions, but the equivalence of discrete particles to oxide inclusions requires further validation. Meanwhile, many particles must be traced to guarantee computational accuracy under complex situations. This makes it difficult to guarantee computational efficiency.

This analysis indicated that there are no robust numerical models with computational accuracy that provide quantitative predictors of the formation and distribution of oxide inclusion defects during cast-filling processes. Therefore, a formation rate model that is relevant to the volume fraction of the liquid metal, the temperature, and the current oxide inclusion density is proposed here. This was based on an in-depth investigation of the oxide inclusion mechanism during cast-filling. A boundary condition was developed to handle the adhesion and accumulation on the wall. This work used the CFD software OpenFOAM for the relevant solver.

To prove the veracity and practicability of the model, we first simulated a representative aluminum alloy casting technology. This was used to analyze the effect of different runner systems on the oxide inclusion distributions inside casting and on the wall. The simulation results were compared with experimental data from the literature. Next, a practical copper alloy casting technology was calculated, and the simulation results of oxide inclusion defects on different parts of the wall were compared to the actual casting defect distribution.

2. Mathematical and numerical modeling

2.1. Evaluation mechanism of oxide inclusion

In most cast-filling processes, the liquid metal has a large area contact with the air. An oxidation reaction between the hot liquid metal and the air is inevitable—especially for the alloys with strong oxidability such as aluminum alloy and copper alloy. When the liquid front has accumulated sufficient oxide inclusions, the oxidation reaction between the liquid metal and the air will stop by the oxide inclusions generated between them. This results in a relatively smooth filling process. However, there is a relatively disorganized filling process due to the fluctuation in the liquid front. A portion of the oxide inclusion collides with the mold and then adheres to it. Another portion of the generated oxide inclusion is then drawn into the liquid metal, and this follows the liquid flow. When the arrangement of the pouring system is unreasonable or the filling process is too disorganized, the resulting oxide inclusion cannot be effectively intercepted by the pouring system. This seriously affects the surface quality and mechanical properties.

2.2. Formation rate model of oxide inclusion

Calculating the oxide inclusion formation rate is one of the keys to accurately predicting oxide inclusion defects. Taking a single simulation element as an object, the formation process of oxide inclusion can be regarded as a chemical reaction process between the liquid metal and the air in the element. When the element is full of liquid metal or air, the formation rate is considered to be zero. There are larger formation rates at higher temperatures. The current oxide inclusion in the element can block the continued formation of oxide inclusions. Consequently, from the point of

numerical simulation, the dominant factors affecting the formation rate S_χ (kg/m^3/s) of oxide inclusion include: element volume fraction of liquid metal α, element temperature T (°C) and element current oxide inclusion density $\chi_{current}$ (kg/m^3).

The reaction rate formula [20] is adopted for the chemical combustion solver in OpenFOAM and measures the effect of volume fraction of liquid metal on the formation rate:

$$\dot{\omega}_{fuel} = -C\bar{\rho}\frac{\varepsilon}{k}\min\left(\tilde{Y}_{fuel}, \frac{\tilde{Y}_{ox}}{N}\right) \quad (1)$$

Here, $\dot{\omega}_{fuel}$ is the reaction rate, kg/m^3/s; C is the model constant; $\bar{\rho}$ is the element average density, kg/m^3; k is the Favre-averaged turbulent kinetic energy per unit mass, m^2/s^2; ε is the dissipation of the Favre-averaged turbulent kinetic energy per unit mass, m^2/s^3; $\tilde{Y}_{fuel}$ and $\tilde{Y}_{ox}$ are the element volume fraction of fuel and oxygen; and N is the stoichiometric required oxygen in kilograms to burn one kilogram of the fuel.

Eq. (1) shows that the reaction rate is maximized when the chemical components are all sufficient. Thus, the formula below is developed to represent the effect of the element volume fraction of liquid metal α on S_χ:

$$S_\alpha = \alpha(1-\alpha) \quad (2)$$

The core gas formation rate (Arrhenius equation [21]) was used to study the effect of temperature on formation rate:

$$K = Ae^{-E/RT} \quad (3)$$

Here, K is the core gas formation rate; A is the pre-exponential factor; E is the apparent activation energy; and R is the molar gas constant.

Eq. (3) shows that the chemical reaction rate has an exponential relationship with temperature. The formula below is developed to represent the effect of the temperature T on S_χ:

$$S_T = e^{1-\frac{1}{\max\left(T-T_{solid}/T_{liquid}-T_{solid},\ 10^{-6}\right)}} \quad (4)$$

Here, T_{solid} and T_{liquid} are the solidus and liquidus temperature of the casting metal, °C.

The formula below is developed to represent the effect of the current oxide inclusion density $\chi_{current}$ on S_χ:

$$S_{\chi_{current}} = \max\left(\frac{\chi_{critical}-\chi_{current}}{\chi_{critical}},\ 0\right) \quad (5)$$

Here, $\chi_{critical}$ is the element critical density of oxide inclusion, kg/m^3. It should be confirmed experimentally.

By combining Eqs. (2), (4) and (5), the element formation rate model of oxide inclusion can be obtained by:

$$\begin{aligned} S_\chi &= A_\chi S_\alpha S_T S_{\chi_{current}} \\ &= A_\chi \alpha(1-\alpha)e^{1-\frac{1}{\max\left(T-T_{solid}/T_{liquid}-T_{solid},\ 10^{-6}\right)}}\max(\chi_{critical} \\ &\quad -\chi_{current}/\chi_{critical},\ 0) \end{aligned} \quad (6)$$

Here, A_χ is the constant of oxide inclusion formation rate, kg/m^3/s. It should be confirmed during practical production.

2.3. Handling adhesion on the wall

During the cast-filling process, oxide inclusions will immediately adhere to the wall of the mold. Once it touches the wall, the oxide inclusion will then influence subsequent cumulative processes. Fig. 2 is a schematic diagram of the adhesion and accumulation of oxide inclusions on the wall. Therefore, one must solely consider the adhesion and accumulation of oxide inclusion on the wall. From the view of numerical simulation, oxide inclusions

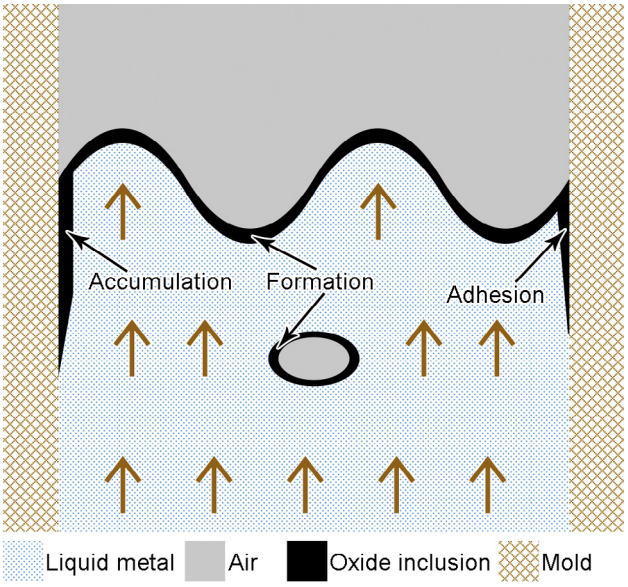

Fig. 2. A schematic diagram of adhesion and accumulation of oxide inclusion on the wall.

on the adjacent element will adhere to the wall stepwise. It cannot accumulate on the wall when the oxide inclusion density on the wall exceeds the critical value. The formula below controls the oxide inclusion distribution on the wall in this paper:

$$\chi_{walNext} = \chi_{wallCurrent} + \chi_{wallCell}\cdot\max\left(\frac{\chi_{wallCritical}-\chi_{wallCurrent}}{\chi_{wallCritical}},\ 0\right) \quad (7)$$

Here, $\chi_{wallNext}$ is the oxide inclusion density on the wall at the next moment, kg/m^3; $\chi_{wallCurrent}$ is the oxide inclusion density on the wall at the current moment, kg/m^3; $\chi_{wallCell}$ is the adjacent element oxide inclusion density at the current moment, kg/m^3; $\chi_{wallCritical}$ is the critical oxide inclusion density on the wall and should be confirmed experimentally, kg/m^3.

2.4. Tracking oxide inclusion movement and calculation methodology

Before explaining the oxide inclusion movement, further, we highlight some assumptions of the models. (1) Wall areas with the same critical oxide inclusion densities have identical adhesive capacity and oxide inclusion limitations. (2) The oxide inclusions inside the liquid metal follow the liquid flow. They have no effect on it. (3) After the casting is removed from the mold, the oxide inclusion that adhered to the wall of mold will stick on the casting surface.

The movement of the oxide inclusion inside the casting is tracked by the transport equation after accessing the formation rate model of oxide inclusion and the adhesion model on the wall:

$$\frac{\partial\chi}{\partial t} + \nabla\cdot(\vec{U}) = S_\chi \quad (8)$$

Here, χ is the elemental oxide inclusion density, kg/m^3; t is the time, s; and $\vec{U}$ is the element velocity, m/s. The quantitative indicator χ reflects the content of oxide inclusion defects in different parts of the system. Before numerical calculations of the cast-filling process, the mold cavity was thought to be filled with air. There were no the oxide inclusion defects on the wall.

Eq. (7) is a boundary condition of the oxide inclusion density field. Implementation of the calculation code is based on the solver interFoam [22] in OpenFOAM. We note that solving the element-centered fields and setting boundary conditions are handled

separately in OpenFOAM. The values of the element center and the boundary center are both recorded in the result files. Consequently, the governing equations of temperature [23] and oxide inclusion (Eqs. (6) and (8)) are added to the foundation of interFoam. This is used to solve the element-centered values of temperature and oxide inclusion. The user-defined boundary condition of oxide inclusion is defined according to Eq. (7). This is used to update the oxide inclusion distribution on the wall. We used the PIMPLE algorithm [24] in the coupled solution of pressure and velocity. This was used for temperature and oxide inclusion fields, and the general calculation process is shown in Fig. 3.

3. Results and discussion

These mathematical and numerical models can predict oxide inclusion defects inside the casting and on the wall during filling. To validate the model, we first calculated a representative aluminum alloy casting technology and analyzed the effect of different runner systems on oxide inclusion distributions. The simulation results were compared to experimental data from the literature. Second, a practical copper alloy casting technology was simulated, and the simulation results of oxide inclusion defects were compared to the actual defect distribution. The mesh generation tool is ICEM CFD [25], and the open source software ParaView [26] was used for post-processing.

3.1. Calculation and verification of aluminum alloy casting oxide inclusion defects under different runner systems

Ingate velocity has a significant impact on the generation of surface turbulence and oxide inclusion entrainment during aluminum alloy casting. A representative aluminum alloy casting technology [12] was chosen here, including a runner and a mold cavity (Fig. 4). Two different runner systems—a Rectangle Runner (RR) and a Vortex-flow Runner (VR) were designed—to achieve different ingate velocities. In comparison to the RR, the VR plays a more effective role in reducing surface turbulence. This ensures that the ingate velocity is less than the critical velocity of 0.5 m/s [5]. We note that the only difference between the two runner systems is the cross-sectional shape of the runners. The cross-sectional area remains the same. This arrangement allows for a direct comparison of the liquid metal flow behavior and the oxide inclusion defects of the castings acquired using different flow mode.

We directly compared the effects of different free surface shapes on oxide inclusion defects. Different runner systems were distinguished by setting different ingate velocities [12]; therefore, the calculation domain is a cuboid area 200 mm × 100 mm × 10 mm (Fig. 4). Table 1 contains the parameters needed for simulation. The aluminum alloy material is LM25 (Al-7Si-0.4Mg). Constant parameters were used to ensure computing efficiency because the cast-filling process was short, and the change in liquid metal temperature remained small.

Figs. 5 and 6 are the volume fraction of liquid metal and oxide inclusion density distributions on the middle cross-section under

Table 1
The parameters needed for simulation.

Parameter	Value
Aluminum alloy density (kg/m^3)	2416
Air density (kg/m^3)	1
Aluminum alloy dynamic viscosity (Pa·s)	1.38e−3
Air dynamic viscosity (Pa·s)	1e−5
Aluminum alloy-air surface tension coefficient (N/m)	0.87
Aluminum alloy specific heat (kJ/kg/K)	1.19
Aluminum alloy heat conductivity (W/m/K)	70.15
Aluminum alloy liquidus temperature (°C)	611
Aluminum alloy solidus temperature (°C)	550
Aluminum alloy latent heat (kJ/kg)	358
Acceleration of gravity (m/s^2)	{0, 0, −9.8}
Ingate velocity (m/s)	RR: {0, 0, 0.7}; VR: {0, 0, 0.4}
Ingate temperature (°C)	740
Constant of oxide inclusion formation rate (kg/m^3/s)	20
Element critical density of oxide inclusion (kg/m^3)	1
Critical oxide inclusion density on the wall (kg/m^3)	2

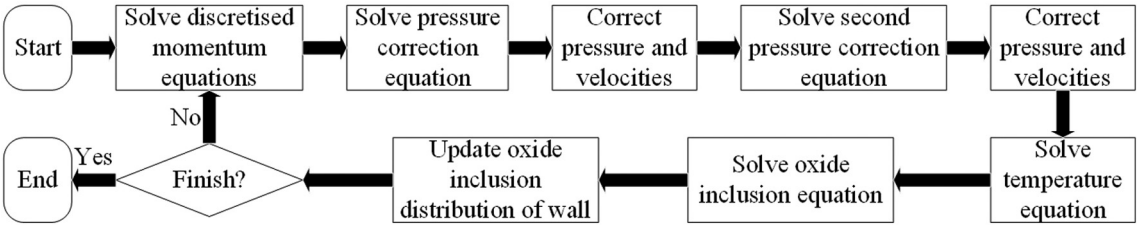

Fig. 3. The general calculation process used in this paper.

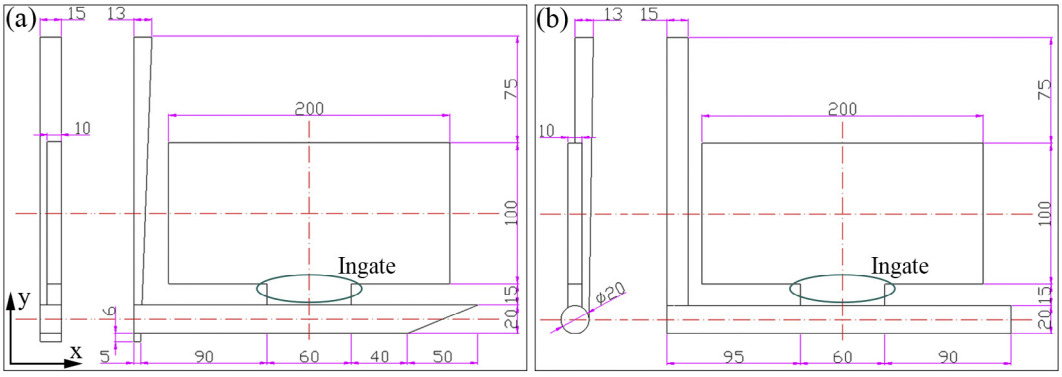

Fig. 4. A representative aluminum alloy casting technology [12] (unit: mm): (a) RR system; (b) VR system.

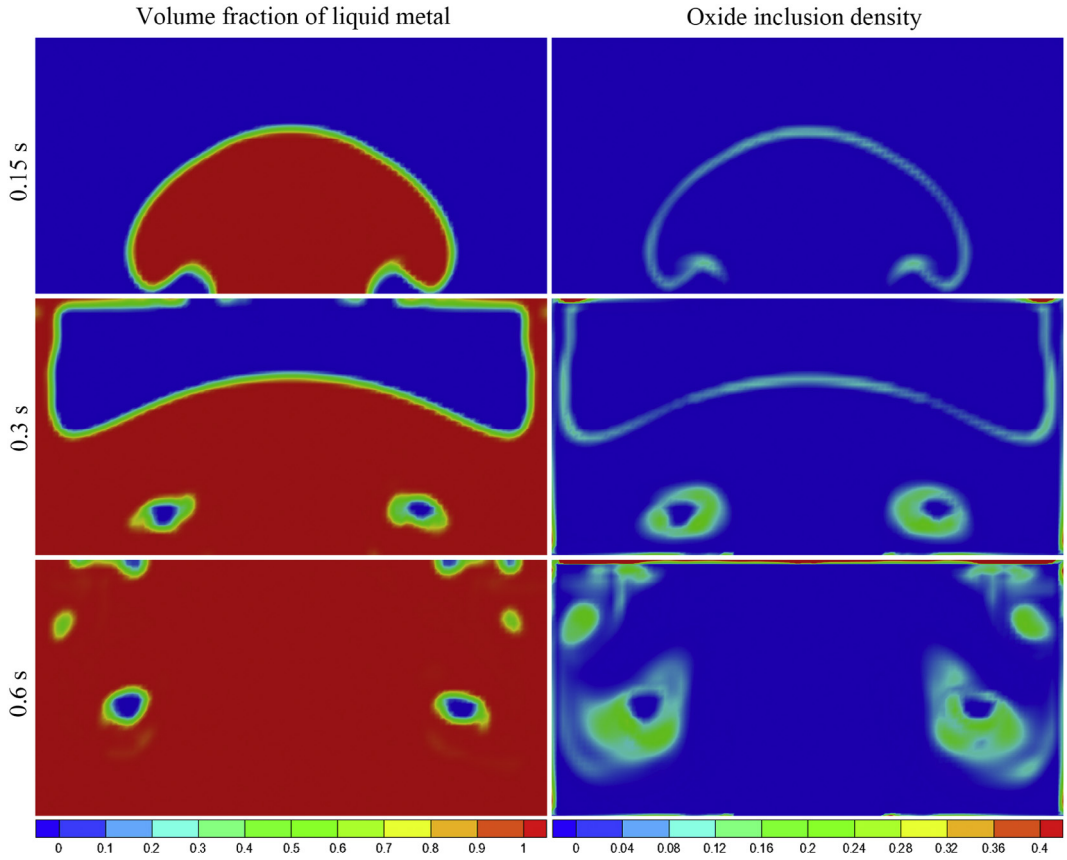

Fig. 5. The volume fraction of liquid metal and oxide inclusion density distributions on the middle cross-section under RR at different times (unit: kg/m^3).

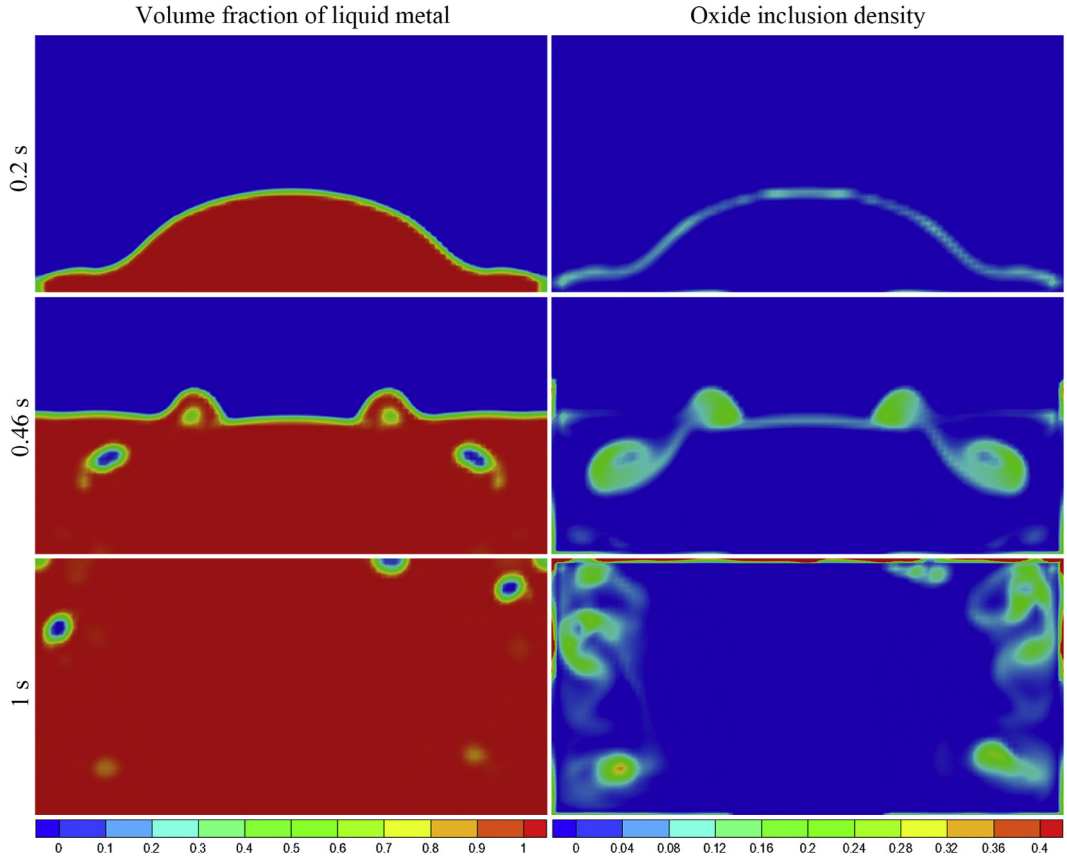

Fig. 6. The volume fraction of liquid metal and oxide inclusion density distributions on the middle cross-section under VR at different times (unit: kg/m^3).

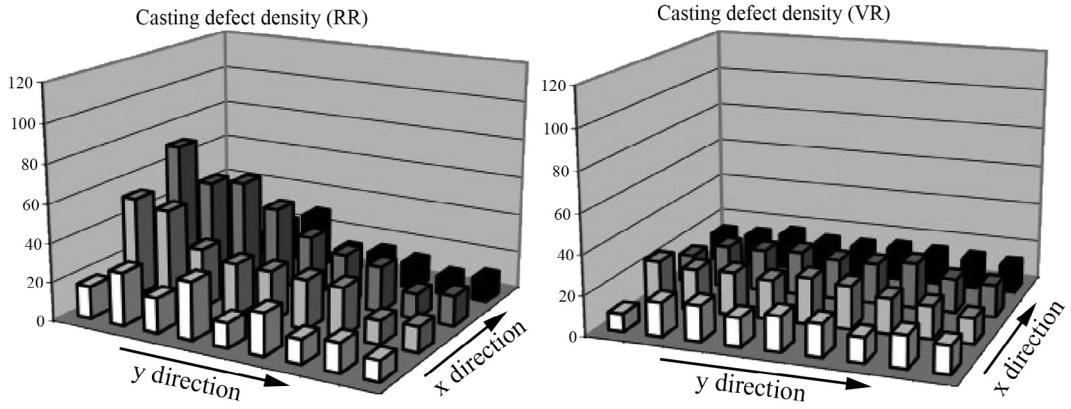

Fig. 7. The distributions of casting defect density (number per unit area) on casting plates under different runners [12].

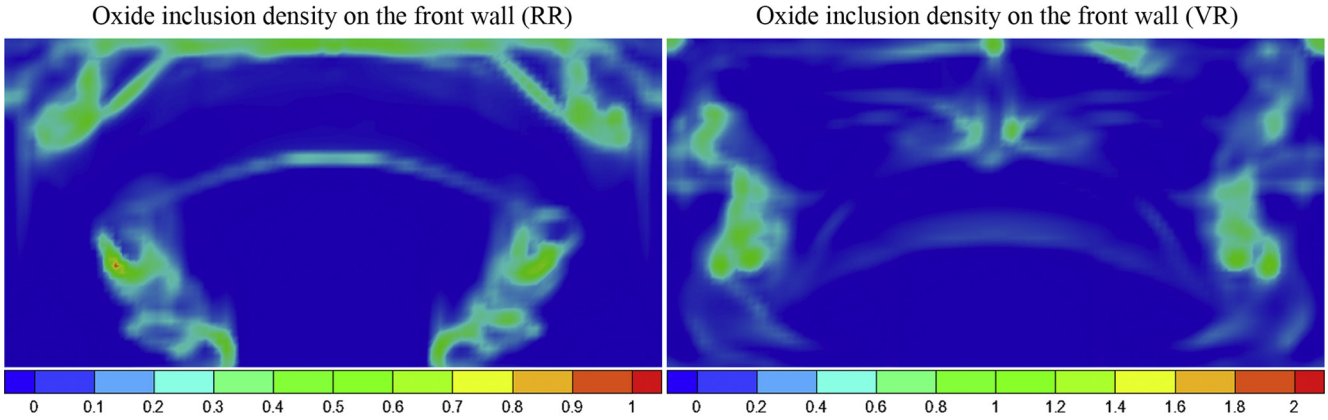

Fig. 8. The oxide inclusion density distributions on the front wall of the casting plates under different runners (unit: kg/m^3).

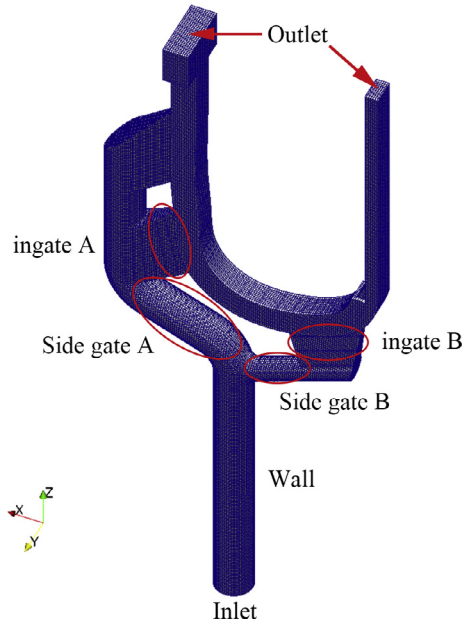

Fig. 9. The geometric model and mesh of the adopted LPDC technology.

Table 2
The parameters needed for the calculation.

Parameter	Value
Copper alloy density (kg/m^3)	7000
Air density (kg/m^3)	1
Copper alloy dynamic viscosity (Pa·s)	3.22e−3
Air dynamic viscosity (Pa·s)	1e−5
Copper alloy-air surface tension coefficient (N/m)	1.2
Copper alloy specific heat (kJ/kg/K)	0.48
Copper alloy heat conductivity (W/m/K)	120
Copper alloy liquidus temperature (°C)	921.4
Copper alloy solidus temperature (°C)	890
Copper alloy latent heat (kJ/kg)	153
Acceleration of gravity (m/s^2)	{0, 0, −9.8}
Inlet pressure	0 s 0 bar; 5 s 0.36 bar; 10 s 0.36 bar
Inlet temperature (°C)	1015
Constant of oxide inclusion formation rate (kg/m^3/s)	10
Element critical density of oxide inclusion (kg/m^3)	1
Critical oxide inclusion density on the wall (kg/m^3)	2

different runners. The volume fraction distributions in Fig. 5 shows that the liquid metal was sprayed from the ingate because of the bigger ingate velocity. Then, two large pieces of entrapped air were formed at both sides of the ingate. These were still at the lower middle of the casting plant. They remained here until the liquid metal filled the top. The oxide inclusion density distributions showed that the oxide inclusions only existed on the liquid front before the appearance of entrapped air. The oxide inclusion was then involved in the liquid metal due to the entrapped air and the inordinate flow pattern. These were mainly distributed at the lower middle of the casting plant. The simulation results in Fig. 6 show that the shape of the liquid metal was smooth under the

VR. The phenomenon of entrapped air was not serious, and the oxide inclusion inside the casting plate was low. These were mainly distributed on either side.

The casting plates acquired under different runners have been polished in Ref. [12]. Thus, image analysis of the defects in the casting plates used the difference in brightness because the casting defects appear much darker than their surrounding phases. This was confirmed in gray scale. The casting defect density (number per unit area) distributions on the casting plates with different runners are shown in Fig. 7. We note that the experimental quantitative analysis of casting defects shown here include all the casting defects such as gas pores, shrinkage pores, and oxide inclusion defects. Thus, the casting defect density and the oxide inclusion density were not identical. However, Fig. 7 shows that the casting defect density distribution under the RR was non-uniform and mainly in the lower middle of the casting plant. The distribution under the VR was uniform.

Fig. 8 shows the oxide inclusion density distributions on the front wall of the casting plates under different runners. The oxide inclusion distribution under the RR was non-uniform and mainly at the lower middle of the plant. The inclusions were on both sides of the plate under the VR. These simulation results show that the shape of the liquid metal was inordinate under the RR relative to the VR. This makes the oxide inclusion defects more serious. The experimental data yielded essentially the same conclusion.

3.2. Calculation and experimental analysis of copper alloy casting oxide inclusion defects

The filling and oxide inclusion evolution processes of a practical copper alloy casting technology were calculated to further validate the utility of the model. The simulation results were compared to the actual casting defect distribution. Fig. 9 shows the geometric model and mesh of the adopted LPDC (low pressure die casting)

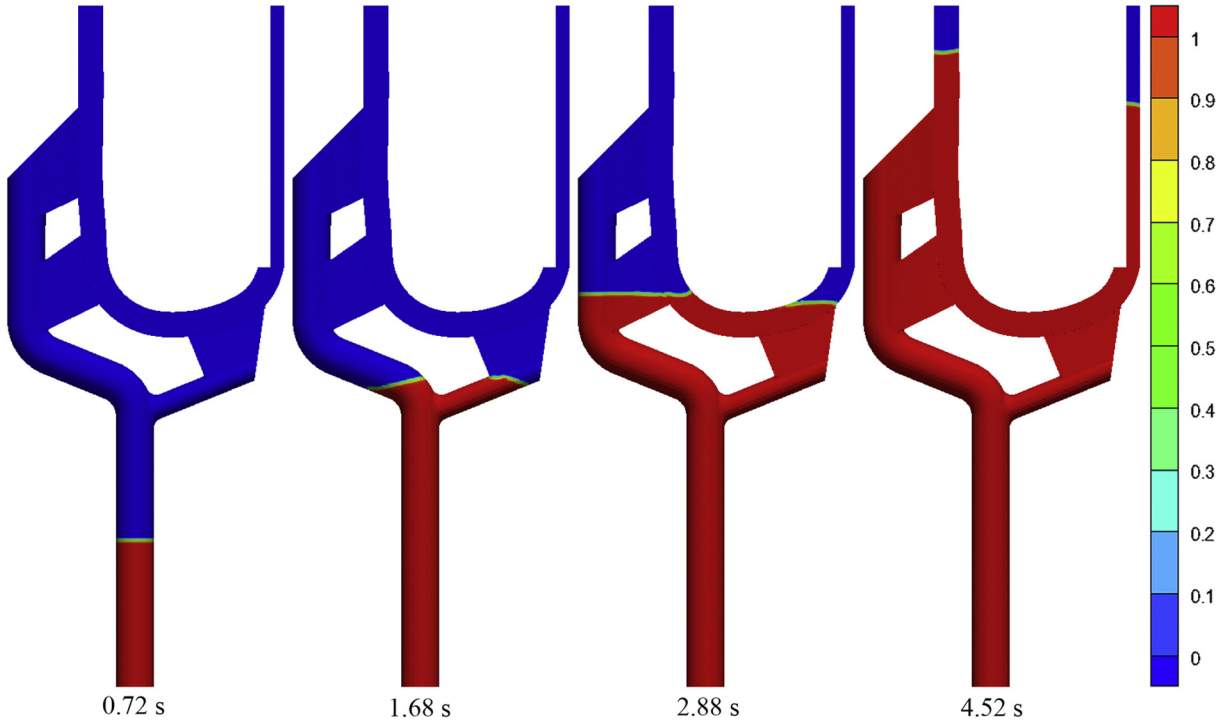

Fig. 10. The liquid metal distributions at different times during filling.

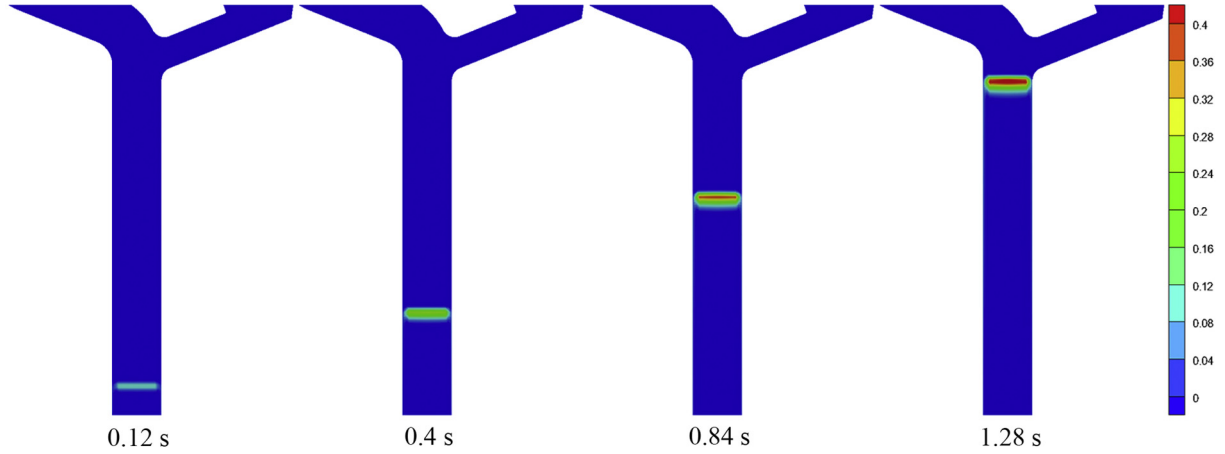

Fig. 11. The oxide inclusion density distributions on the middle cross-section when the liquid metal flowed into the lift tube (unit: kg/m^3).

technology. The overall dimensions of the casting are 217 mm × 50 mm × 535 mm. The top of the casting has a curved tubular construction with a thickness of 4 mm. Table 2 shows the parameters needed for this calculation. The copper alloy material is GKMS60.

The liquid metal distributions as a function of time during the filling process are shown in Fig. 10. The filling process was smooth with a slow upward inlet pressure in the LPDC. This made the oxide inclusion defect concentrated on the liquid front. Fig. 11 shows the oxide inclusion density distributions on the middle cross-section when liquid metal flowed in the lift tube. The simulation results indicate that the production of oxide inclusion gradually increased with air exposure time. This is because only the liquid metal around the front touched the wall of the lift tube; the oxide inclusion around the front almost adhered to the adjacent wall.

This analysis shows that oxide inclusions had difficulties becoming involved in the liquid metal during the smooth filling process. As a result, most oxide inclusions adhered to the wall of mold. Four key parts of this casting technology were selected and were used to analyze oxide inclusion defects on different parts of the wall: side gate A, side gate B, ingate A, and ingate B (Fig. 9). A comparison between the oxide inclusion defects on the wall and the casting surface morphology on different parts is shown in Fig. 12. At first, we note that the "filling-solidification-picking up" process was done more than once for the same mold. This causes the oxide inclusion to repeatedly accumulate on the wall. The casting surface morphology is significantly influenced after the accumulation achieved a certain level. Thus, the casting surface morphology can directly reflect the situation of the oxide inclusion defect on the wall. To further explain how the accumulation of oxide inclusions generated the coarse casting surface area, two locations on the casting gate were chosen for energy dispersive spectrum (EDS) analysis (Fig. 12). The results are shown in Fig. 13 and indicate that the oxygen content on the coarse casting surface area is larger than other areas; hence, we verified that the coarse casting surface area was generated during accumulation of oxide inclusions.

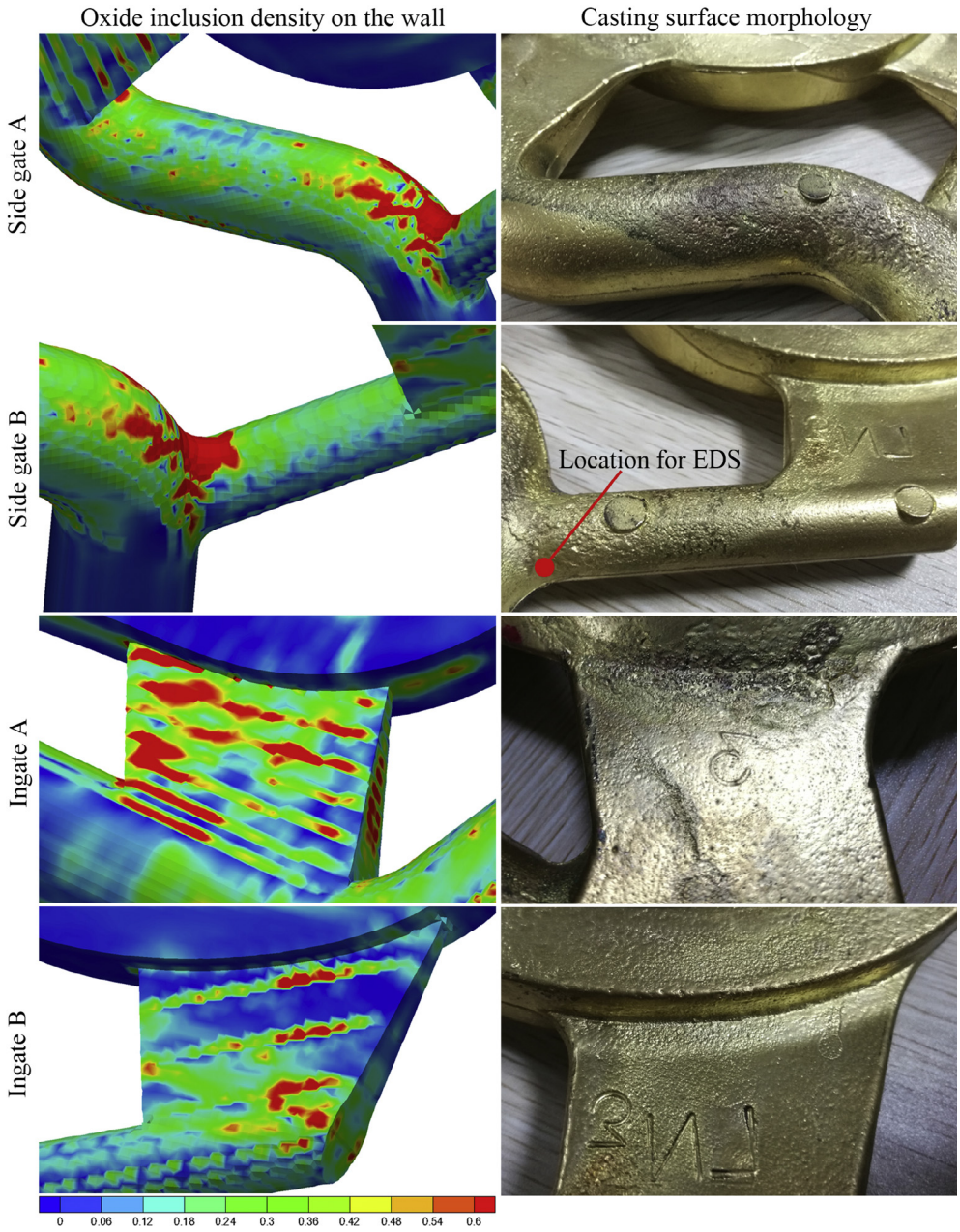

Fig. 12. Comparison between the oxide inclusion defect on the wall and the casting surface morphology on different parts (unit: kg/m^3).

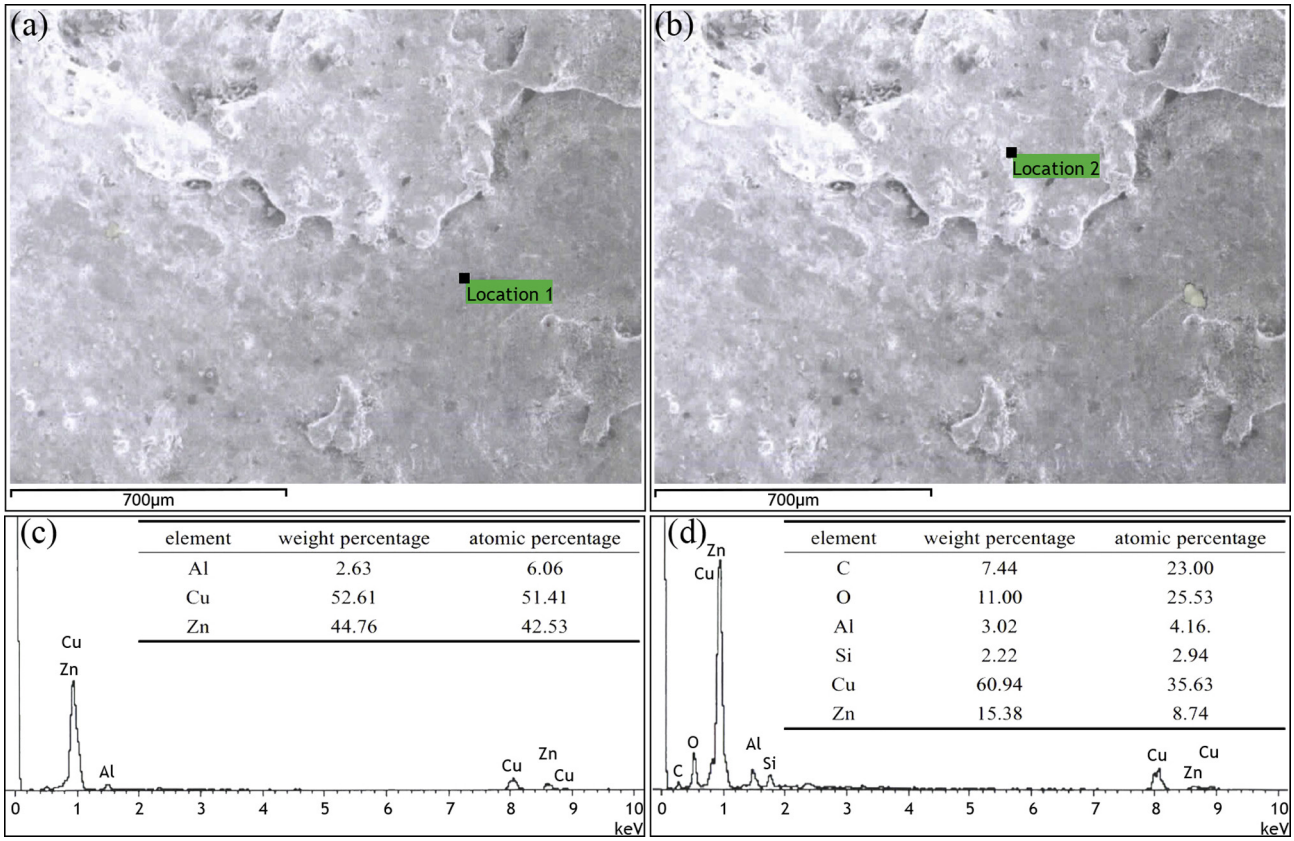

Fig. 13. Energy dispersive spectrum (EDS) analysis results of the chosen locations: (a) location 1 for EDS; (b) location 2 for EDS; (c) EDS result of location 1; and (d) EDS result of location 2.

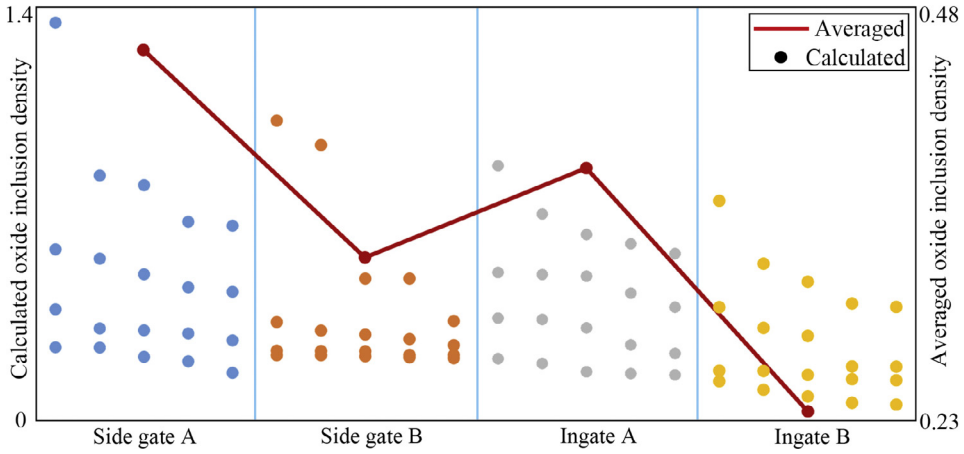

Fig. 14. The calculated and averaged oxide inclusion density on the wall of evenly distributed positions on different parts (unit: kg/m^3).

Oxide inclusions were generated when the liquid front flowed in the lift tube, and only bits of the oxide inclusion adhered to the wall (Fig. 12). Thus, some oxide inclusions directly touched the wall when the liquid front flowed to the side gates. This caused the oxide inclusions to adhere to side gates A and B. These were concentrated on the top of the side gates because side gate A has a bigger diameter than side gate B. Thus, more oxide inclusions flowed into side gate A resulting in more oxide inclusion on ingate A than on ingate B.

Next, twenty positions evenly distributed on each part were selected to record the oxide inclusion density values. The goal was to quantitatively analyze the oxide inclusion distribution of the four key parts (Fig. 14). The comparison results indicate that the oxide inclusion density of side gate A was the biggest. Side gate B was bigger in a few areas; the oxide inclusion defect of ingate A was more serious than ingate B. On average, the simulation results of the oxide inclusion defects were consistent with the actual casting defect distribution. This certifies the practicability of the adopted model.

4. Conclusions

(1) We report a formation rate model that is relevant to the volume fraction of liquid metal, the temperature, and the current oxide inclusion density. It predicts oxide inclusion

defects during cast-filling processes. A boundary condition was developed to handle the adhesion and accumulation of oxide inclusions on the wall. This is a quantitative indicator of oxide inclusion defects in different parts. We used interFoam solver in OpenFOAM to predict oxide inclusion defects inside the casting and on the walls.

(2) The quantitative model of oxide inclusions had multiple parameters: a rate constant of oxide inclusion formation, the element critical density of oxide inclusion, and the critical oxide inclusion density on the wall. These should be determined empirically.

(3) A representative aluminum alloy casting technology was used to analyze the effect of different runner systems on the oxide inclusion distribution inside casting and on the wall. The simulation results basically coincide with the experimental results from the literature.

(4) A practical copper alloy casting technology was calculated, and the simulation results of oxide inclusion defects on different parts of the wall are consistent with the actual casting defect distribution. This certifies the utility of the model.

Conflict of interest

We declare that we have no financial and personal relationships with other people or organizations that can inappropriately influence the work submitted.

Acknowledgements

This research is supported by the Program for New Century Excellent Talents in University (NCET-13-0229) and the National Science & Technology Key Projects of Numerical Control (2012ZX04010-031).

Appendix A. Supplementary material

Supplementary data associated with this article can be found, in the online version, at https://doi.org/10.1016/j.ijheatmasstransfer.2017.11.127.

References

[1] L. Liu, A.M. Samuel, F.H. Samuel, et al., Influence of oxides on porosity formation in Sr-treated Al-Si casting alloys, J. Mater. Sci. 38 (6) (2003) 1255–1267.
[2] S.G. Liu, F.Y. Cao, X.Y. Zhao, et al., Characteristics of mold filling and entrainment of oxide film in low pressure casting of A356 alloy, Mater. Sci. Eng., A 626 (2015) 159–164.
[3] Y.D. Kwon, Z.H. Lee, The effect of grain refining and oxide inclusion on the fluidity of Al–4.5 Cu–0.6 Mn and A356 alloys, Mater. Sci. Eng., A 360 (1) (2003) 372–376.
[4] X. Cao, J. Campbell, Oxide inclusion defects in Al-Si-Mg cast alloys, Can. Metall. Quarter. 44 (4) (2005) 435–448.
[5] J. Campbell, The modeling of entrainment defects during casting, Simul. Alumin. Shape Cast. Process.: Alloy Des. Mech. Proper. (2006) 123–132.
[6] J. Runyoro, S.M.A. Boutorabi, J. Campbell, Critical gate velocities for film-forming casting alloys: a basis for process specification, AFS Trans. 100 (1992) 225–234.
[7] W. Sun, P. Scarber, H. Li, et al., Modeling, model verification, and defect formation in iron castings, Keith Millis Symposium on Ductile Cast Iron, 2003, pp. 1–12.
[8] MAGMASOFT Company, MAGMASOFT V4.4 Manual, 2005.
[9] H.D. Zhao, I. Ohnaka, Numerical simulation of oxide entrapment and mold filling process of Al casting, Chin. J. Nonferr. Metals 15 (8) (2005) 1200–1207.
[10] H. Zhao, I. Ohnaka, Y. Sako, et al. Estimation of porosity defects with consideration of oxide entrapment, in: Proceedings of the 65th World Foundry Congress, 2002, pp. 749–754.
[11] J. Lin, M. Sharif, Numerical simulation of the movement, breakup and entrapment of oxide films during aluminum casting, Alumin. Trans. 1 (1) (1999) 71–78.
[12] X. Yang, X. Huang, X. Dai, et al., Numerical modelling of entrainment of oxide film defects in filling of aluminium alloy castings, Int. J. Cast Met. Res. 17 (6) (2004) 321–331.
[13] X. Dai, X. Yang, J. Campbell, et al., Effects of runner system design on the mechanical strength of Al-7Si-Mg alloy castings, Mater. Sci. Eng., A 354 (1) (2003) 315–325.
[14] N.W. Lai, W.D. Griffiths, J. Campbell, Modelling of the potential for oxide film entrainment in light metal alloy castings, Model. Cast. Weld. Adv. Solidificat. Process. (2003) 415–422.
[15] M.R. Barkhudarov, C.W. Hirt, Tracking defects, Die Cast. Eng. 43 (1) (1991) 44–52.
[16] G. Backer, C.W. Kim, K. Siersma, et al., Computational analysis of oxide Inclusions in aluminum castings, Simul. Alumin. Shape Cast. Process.: Alloy Des. Mech. Proper. (2006) 165–175.
[17] C. Reilly, N.R. Green, M.R. Jolly, et al., The modelling of oxide film entrainment in casting systems using computational modelling, Appl. Math. Model. 37 (18) (2013) 8451–8466.
[18] Y.J. Xu, M. Yu, Numerical simulation of inclusion movement in mold filling process of metal melt, J. Shenyang Univ. Technol. 29 (4) (2007) 392–395.
[19] X. Dai, X. Yang, J. Campbell, et al., Influence of oxide film defects generated in filling on mechanical strength of aluminium alloy castings, Mater. Sci. Technol. 20 (4) (2004) 505–513.
[20] H.I. Kassem, K.M. Saqr, H.S. Aly, et al., Implementation of the eddy dissipation model of turbulent non-premixed combustion in OpenFOAM, Int. Commun. Heat Mass Transfer 38 (3) (2011) 363–367.
[21] K.J. Laidler, The development of the Arrhenius equation, J. Chem. Educ. 61 (6) (1984) 494–498.
[22] OpenFOAM Foundation Ltd., OpenFOAM User Guide V4.0, 2016.
[23] L. Cao, D.M. Liao, Y.Z. Lu, et al., Heat transfer model of directional solidification by LMC process for superalloy casting based on finite element method, Metall. Mater. Trans. A 47 (9) (2016) 4640–4647.
[24] Tobias Holzmann, Mathematics, Numerics, Derivations and OpenFOAM(R), 4th ed., Holzmann CFD, Leoben, 2017.
[25] X. Lei, L. Huixin, The technology of numerical simulation based on ANSYS ICEM CFD and CFX software, Mech. Eng. 12 (2008) 65–66.
[26] A. Henderson, J. Ahrens, C. Law, The ParaView Guide, 2004.